Magnetic Resonance in Medicine

Fundamentals of turbulent flow spectrum imaging

Hannes Dillinger [iD] | **Charles McGrath** [iD] | **Christian Guenthner** [iD] |
Sebastian Kozerke [iD]

Institute for Biomedical Engineering, University and ETH Zurich, Zurich, Switzerland

Correspondence
Hannes Dillinger, Institute for Biomedical
Engineering, University and ETH
Zurich, Gloriastrasse 35, 8092 Zurich,
Switzerland.
Email: dillinger@biomed.ee.ethz.ch

Purpose: To introduce a mathematical framework and in-silico validation of turbulent flow spectrum imaging (TFSI) of stenotic flow using phase-contrast MRI, evaluate systematic errors in quantitative turbulence parameter estimation, and propose a novel method for probing the Lagrangian velocity spectra of turbulent flows.

Theory and Methods: The spectral response of velocity-encoding gradients is derived theoretically and linked to turbulence parameter estimation including the velocity autocorrelation function spectrum. Using a phase-contrast MRI simulation framework, the encoding properties of bipolar gradient waveforms with identical first gradient moments but different duration are investigated on turbulent flow data of defined characteristics as derived from computational fluid dynamics. Based on theoretical insights, an approach using velocity-compensated gradient waveforms is proposed to specifically probe desired ranges of the velocity autocorrelation function spectrum with increased accuracy.

Results: Practical velocity-encoding gradients exhibit limited encoding power of typical turbulent flow spectra, resulting in up to 50% systematic underestimation of intravoxel SD values. Depending on the turbulence level in fluids, the error due to a single encoding gradient spectral response can vary by 20%. When using tailored velocity-compensated gradients, improved quantification of the Lagrangian velocity spectrum on a voxel-by-voxel basis is achieved and used for quantitative correction of intravoxel SD values estimated with velocity-encoding gradients.

Conclusion: To address systematic underestimation of turbulence parameters using bipolar velocity-encoding gradients in phase-contrast MRI of stenotic flows with short correlation times, tailored velocity-compensated gradients are proposed to improve quantitative mapping of turbulent blood flow characteristics.

KEYWORDS
phase-contrast MRI, pulse sequence design, Reynolds stress tensor, turbulent blood flow, turbulent kinetic energy

---

1 | INTRODUCTION

Time-resolved 3D phase-contrast MRI (4D flow MRI) has received significant attention in the field.[1] Applications of 4D flow MRI include the assessment of valve diseases,[2] aortic aneurysms/dissection,[3,4] stenosis of pulmonary vessels,[5] and many more. In aortic valve stenosis, quantification of blood flow jet velocities and maximum pressure gradients play a key role in clinical diagnosis.[6] Moreover, turbulent flow metrics including turbulent kinetic energy (TKE) have been regarded of potential value. Binter et al[7] have demonstrated that increased levels of TKE convey additional information relative to mean pressure gradients across stenoses; thus, potential utility has been indicated for improved assessment of valve diseases.

Considerable research attention has been directed to mapping TKE using 4D flow MRI.[7-9] Moreover, encoding of the full Reynolds stress tensor has been proposed to assess turbulent shear flow and improve the estimation of net pressure losses.[8,10]

The encoding theory of random motion in turbulent flow using MRI is covered in seminal studies by Kuethe et al[11,12] and Gao et al.[13] A theoretical framework has been formulated based on the assumption of an exponentially decaying correlation function, which was applied to map turbulent intensities in a stenosis phantom.[14] Based on this framework, Gatenby and Gore[15,16] differentiated between 2 regimes: $\tau_c \gg \tau$ and $\tau_c \ll \tau$, where the average correlation time τ_c for a fluid element to change direction is related to a *velocity-encoding gradient* (VEG) of duration 2τ.

The assumption $\tau_c \gg \tau$ constitutes the foundation of the work concerned with turbulence encoding.[17,18] However, to the best of our knowledge, this assumption has never been verified for phase-contrast MRI. Whereas in vitro and in vivo measurements[19-21] in stenotic aortae with realistic flow conditions have predicted a correlation time τ_c in the millisecond range, it at the same time invalidates the assumption $\tau_c \gg \tau$ given practical bipolar gradient waveform lobe durations τ.

Of note, early work by Stepišnik[22,23] introduced a description of motion spectra in terms of the velocity auto-correlation function and its Fourier transform for diffusion MRI. The main conclusion derived by Stepišnik is that the attenuation of the magnitude signal solely depends on the area of the overlap of gradient and motion spectra. Callaghan and Stepišnik[24] successfully applied a method using different gradient spectra for predicting the frequency-varying diffusion coefficient in a moving fluid. In turbulent flow MRI, to the best of our knowledge, no such considerations have been made. Newling et al[25] state that the correlation time must be imaged on a voxel basis to obtain precise estimates of the diffusivity; however, although they refer to Gao and Gore's technique, they do not apply it.

The objectives of the current work are threefold: First, the spectral response of motion-encoding gradient waveforms (including velocity-encoding and velocity-compensated waveforms) is derived and evaluated with respect to their theoretical encoding power of characteristic turbulent flow spectra. It is shown that VEGs of identical first-gradient moments but different durations result in different degrees of underestimation of turbulence parameters. Second, a method for quantification of turbulent motion spectra using *velocity-compensated gradients* (VCG) is presented and used to correct for systematic underestimation of turbulence parameters derived from velocity-encoded data. Third, a correction method for turbulence parameter estimation using VEGs with different durations and without prior probing of the turbulent motion spectra is proposed.

2 | THEORY

2.1 | Encoding of incoherent motion using motion-encoding gradients

The k-space signal equation yielding data $d(t)$,

$$d(t) = \int_{\mathscr{V}} \rho_0 \left(\overrightarrow{r'}(t) \right) e^{j\varphi(t)} d\overrightarrow{r'}(t), \tag{1}$$

is based on the Fourier relation of the spatially dependent complex-valued transverse magnetization $\rho_0 \left(\overrightarrow{r'}(t) \right)$ in the excited volume $\mathscr{V}$ given phase,

$$\varphi(t) = \gamma \int_{t_0}^{t} \overrightarrow{G}(t') \cdot \overrightarrow{r'}(t') dt', \tag{2}$$

and evaluated as the time integral of the gradient waveform $\overrightarrow{G}(t)$ and the time-dependent position vector of magnetization $\overrightarrow{r'}(t)$ starting at a reference point in time t_0 (assumed zero for the remainder of the paper). Because the current paper focuses on motion-encoded phase, henceforth $\overrightarrow{G}(t)$ is termed motion-encoding gradient (MEG). Depending on the order of moment compensation, a VEG with vanishing zeroth moment $\overrightarrow{M_0}(TE) = \int_0^{TE} \overrightarrow{G}(t) dt \equiv 0$ or a VCG with vanishing zeroth and first moment $\overrightarrow{M_1}(TE) = \int_0^{TE} \overrightarrow{G}(t)(t - t_0) dt \equiv 0$ with respect to TE is obtained.

2.1.1 | Temporal interpretation

If incoherent motion is present in a voxel, the Fourier phase $\varphi(t)$ results from an ensemble of magnetization, and the signal received can be written as the ensemble average[26]

$$E(t) = \overline{e^{j\varphi(t)}} = \exp\left[\sum_{n=1}^{\infty}\frac{(-1)^n}{n!}\int_0^t\int_0^t\cdots\int_0^t\langle j\varphi(t_1)\,j\varphi(t_2)\cdots j\varphi(t_n)\rangle_c\,dt_1dt_2\cdots dt_n\right],\tag{3}$$

where index c denotes the cumulant average,[27] whereas the volume integral is omitted for brevity. If a Gaussian distribution is assumed (see Appendix), the resulting expression for the signal of an ensemble of magnetization with Gaussian phase distribution is given as

$$E(t) = \exp\left[-j\,\gamma\underbrace{\int_0^t\vec{G}(t')\cdot\overline{\vec{r}(t')}dt'}_{\varphi_0(t)+\varphi_v(t)} - \frac{1}{2}\gamma^2\underbrace{\int_0^t\int_0^t\vec{G}(t_1)\cdot\overline{\vec{r}(t_1)\vec{r}(t_2)}_{LC}\cdot\vec{G}(t_2)\,dt_1dt_2}_{\alpha(t)}\right].\tag{4}$$

Because $\alpha(t)$ in Equation (4) is real valued, it exhibits a damping of the magnitude, which is referred to as dephasing due to intravoxel SD (IVSD[18]).

Performing a per partes integration,[28] Equation (4) results in

$$E(t) = \exp\left[-j\,\gamma\underbrace{\int_0^t\vec{q}(t')\cdot\overline{\vec{v}(t')}dt'}_{\varphi_v(t)} - \frac{1}{2}\gamma^2\underbrace{\int_0^t\int_0^t\vec{q}(t_1)\cdot\overline{\vec{v}(t_1)\vec{v}(t_2)}_{LC}\cdot\vec{q}(t_2)\,dt_1dt_2}_{\alpha(t)}\right],\tag{5}$$

where $\vec{q}(t) = \int_0^t\vec{G}(t')\,dt'$ denotes the time integral of the gradient waveform, and $\vec{v}(t)$ denotes the instantaneous velocity. Of note, the amount of spin ensemble dephasing (ie, the value of $\alpha(t)$) is solely dependent on the ratio of the correlation time scale τ_c (proportional to the term $\overline{\vec{v}(t_1)\vec{v}(t_2)}_{LC}$, further defined in Equation (8)) and the duration τ of the MEG given a fixed encoding strength.

The assumption $\tau_c \gg \tau$ implies that the spectral energy of the random process $\overline{\vec{v}(t_1)\vec{v}(t_2)}_{LC}$ is confined in a low frequency regime compared to the spectrum of the VEG. Therefore, the amount of dephasing given by $\alpha(t)$ in Equation (5) can be controlled by the MEG amplitude alone, independent of duration τ, as long as $\tau_c \gg \tau$ holds. However, satisfying $\tau_c \gg \tau$ for a given correlation time τ_c in the millisecond regime would result in infeasible MEG durations. It can therefore be necessary to operate in the regime $\tau_c \approx \tau$. As can be seen in Figure 1, τ_c may vary spatially and, for pulsatile flow, vary also temporally.
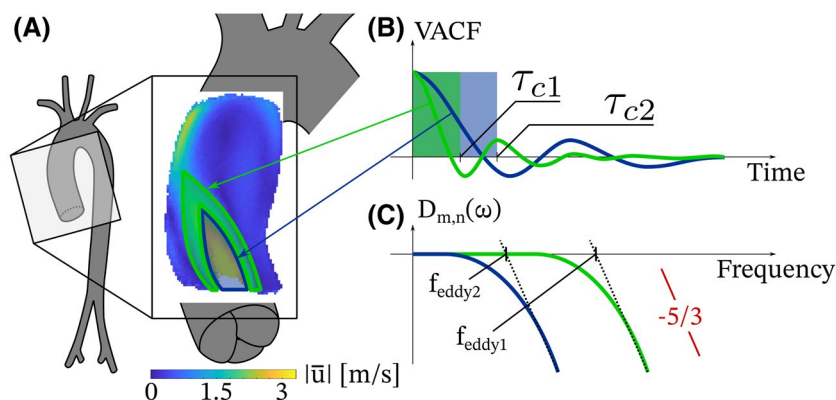

FIGURE 1 (A) Turbulence characteristics in a jet region vary spatially and temporally and can be described by random processes with different properties. Underlying mean velocity magnitude data[56] $|\overline{u}|$ enables differentiation between jet core and boundary zone, for example, which are expected to show different turbulence characteristics (compare TKE plots in Binter et al.[56]). (B) Depending on the region, for example, at the jet boundary, velocity autocorrelation functions exhibit a shorter correlation time τ_{c1} when compared to τ_{c2} in the jet core. (C) This results in different VACF spectra $D_{m,n}(\omega)$, $m, n \in \{x, y, z\}$. The eddy frequency f_{eddy} is used to describe the spectral dynamics of the simplified random processes. $-5/3$ line depicts the begin of the inertial range of the 2 spectra, respectively. f_{eddy}, eddy frequency; TKE, turbulent kinetic energy; VACF, velocity autocorrection function

When neglecting all terms with orders higher than 1 in the expansion of the general distribution, Equation (4) results. The term $\varphi_v(t)$ is the phase component, which encodes bulk motion, whereas the second term $\alpha(t)$ encodes incoherent motion fluctuating around the mean. The tensor property of <u>the product</u> of the vectors $\vec{q}(\tau_1)$, $\vec{q}(\tau_2)$ and the matrix $\vec{v}(\tau_1)\vec{v}(\tau_2)_{LC}$, in theory, enables probing of every element of the matrix by encoding a linear combination <u>of the matrix</u> elements. Because the correlation matrix $\vec{v}(\tau_1)\vec{v}(\tau_2)_{LC}$ is necessarily symmetric, a dataset of 6 orthogonal measurements, that is, a linear combination of the upper or lower triangle, provides all necessary information. ICOSA6,[29] for example, is used to sample the surface of an icosahedron space, which is spanned by the main gradient directions with the necessary 6 measurements. Recent implementations have employed a multi-v_{enc} approach[9] using a set of 3 different v_{enc}'s to account for the nonlinearity in the encoding of $\alpha(t)$ in $E(t)$.

2.1.2 | Spectral interpretation

The velocity autocorrection function (VACF) of a random motion process is defined as

$$VACF(t, \tau) = \overline{\vec{v}(t)\,\vec{v}(t+\tau)} = \int_{lt}^{\infty} \vec{v}(t') \cdot \vec{v}(t'+\tau)\,dt', \quad (6)$$

where $\vec{v}(t)$ is the instantaneous velocity. Given a stationary ergodic random process, temporal and spatial averaging can be exchanged yielding the same result, and only the time interval τ (and not the exact origin of time of the measurement) matters.[26] The VACF can therefore be written as

$$VACF(\tau) = \overline{\vec{v}(0)\,\vec{v}(\tau)}. \quad (7)$$

The correlation time τ_c defines a time scale for the "memory" of the random process[26,30] as

$$\tau_c = \frac{\int_0^{\infty} \overline{\vec{v}(0)\,\vec{v}(t')}\,dt'}{\overline{\vec{v}(0)^2}}. \quad (8)$$

The spectrum of the VACF is given as the Fourier pair

$$D_{m,n}(\omega) = \frac{1}{2}\int_{-\infty}^{\infty} \overline{v_m(0)\,v_n(t')}e^{j\omega t'}dt' = \int_0^{\infty} \overline{v_m(0)\,v_n(t')}e^{j\omega t'}dt', \quad (9)$$

where m, n denote different spatial directions $\{x, y, z\}$ and $D_{m,n}(\omega)$ is also known as the self-diffusion tensor.[26] In the right-most term, the even property of $VACF(\tau)$ is utilized.

Equation (9) can be used to reveal the spectral relationship between the MEG and VACF spectrum, given as $S(\omega, t)$ and $D_{m,n}$, respectively, as

$$\alpha(t) = \frac{1}{2\pi}\gamma^2 \int_{-\infty}^{\infty} D_{m,n}(\omega)\,S(\omega, t)d\omega. \quad (10)$$

Further details about the derivation can be found elsewhere.[28]

The MEG spectrum is given as

$$S(\omega, t) = |\tilde{q}(\omega, t)|^2, \quad (11)$$

where $\tilde{q}(\omega, t) = \int_0^t q(t')\,e^{j\omega t'}dt'$ and $q(t) = \int_0^t G(t')\,dt'$, that is, the Fourier transform of the time integral of gradient waveform samples (see Appendix or Ref. [31]).

From Equation (10), several conclusions can be drawn:

1. The signal attenuation caused by $\alpha(t)$ is determined by the area under the curve that is given by the product of the VACF spectrum $D_{m,n}(\omega)$ and the MEG spectrum, that is, the sensor spectrum $S(\omega, t)$.
2. If the MEG waveform would be an ideal bipolar Dirac function ($\vec{G}(0) = \vec{c}, \vec{G}(\tau) = -\vec{c}, \vec{G}(t) = \vec{0}\ \forall t \setminus \{0, \tau\}$, $\vec{c} \in \mathbb{R}^3$ ie, a VEG waveform), the gradient spectrum $S(\omega, t) = \text{const}\ \forall \omega$, which hence permits probing the entire VACF spectrum. This can be interpreted as the short gradient pulse approximation[32] in analogy to literature on measuring the diffusion coefficient.[33]
3. If the correlation time is significantly shorter than the time for motion encoding, $\tau_c \ll \tau$, Equation (10) can be approximated[23] as

$$\alpha(t) = \frac{1}{2\pi}\gamma^2 D_{m,n}(0)\int_{-\infty}^{\infty} S(\omega, t)\,d\omega, \quad (12)$$

which results in the equation derived by Torrey[34] once the Parceval identity[31] is applied

$$\alpha(t) = \gamma^2 D_{m,n}(0)\int_0^t \underbrace{\left|\left|\int_0^u \vec{G}(t')\vec{G}(t')\,dt'\right|\right|^2}_{q(u)} du \quad (13)$$

with $D_{m,n}(0)$ being the self-diffusion coefficient for the directional indices m, n, which is not dependent on ω because $D_{m,n}(\omega) \approx D_{m,n}(0)\ \forall \omega$ is assumed.

4. TKE is given as $k = \int_0^{\infty} E_{m,m}(\omega)\,d\omega$, where $E_{m,m}(\omega)$ denotes the energy spectrum,[35] which can be interpreted as the VACF spectrum $D_{m,m}(\omega)$ (further details in the Appendix). Subsequently, only probing of the entire

VACF spectrum in the limit of short gradient pulses results in quantitatively correct estimates of TKE.

5. Different frequency ranges of the VACF spectrum can be probed, if the gradient spectral response is tailored accordingly, potentially allowing reconstruction of the entire VACF spectrum from multiple measurements.

2.1.3 | Relation to turbulence theory

Reynolds decomposition of turbulent velocity fields results in separate mean and fluctuating velocity field components.[35] The fluctuating component can be described by a random process[36] with correlation time τ_c. If $\vec{v}(t)$ is assumed to be the velocity of a fluid particle in the flow field, it is found by inserting VEG waveforms into Equation (5) that $\alpha(t)$ encodes the VACF.[37]

The Reynolds stress tensor (RST) is defined by the covariance of velocity components,

$$RST = \begin{bmatrix} \sigma_{xx}^2 & \sigma_{xy}^2 & \sigma_{xz}^2 \\ \sigma_{yx}^2 & \sigma_{yy}^2 & \sigma_{yz}^2 \\ \sigma_{zx}^2 & \sigma_{zy}^2 & \sigma_{zz}^2 \end{bmatrix}, \tag{14}$$

where $\sigma_{mn}^2 = \langle u_m u_n \rangle$, $m, n \in \{x, y, z\}$.[35] The definition of the covariance of the velocity

$$\langle u_m u_n \rangle = \overline{u_m u_n} - \overline{u_m}\,\overline{u_n}, \tag{15}$$

directly connects the RST to the location correlation (denoted in Equation (4) and defined in the Appendix) when using VEGs.

2.2 | Spectra of VEG and VCG

The gradient spectra $S(\omega, t)$ for VEGs with identical first gradient moment $M_1 = \pi / (\gamma v_{enc})$ for $v_{enc} = 450$ cm/s (used in recent works[9]) but different frequencies are shown in Figure 2A. The VEG waveforms respect the gradient limit specifications given in the Methods section.

The gradient spectrum of a VEG with duration 2τ and $f_{VEG} = 1/(2\tau)$ is characterized by a *sinc* function with the first zero crossing at $f_0 = 2f_{VEG}/N$ (Figure 2B), where N is the number of repetitions. In general, the zero-frequency lobe is always dominant.

In Figure 2C, VCG gradient waveforms for a different number of repetitions but constant frequency f_{VCG} are

FIGURE 2 Gradient waveforms and spectra for (A, B) VEG ($v_{enc} = 450$ cm/s, $f_{VEG} = \{500, 1000, 1200\}$Hz), and (C, D) VCG ($f_{VCG} = 1000$ Hz, $N_{f_{VCG}} = \{2, 5, 10\}$). The spectra plots are calculated according to Equation (11) and are normalized by their value at $f = 0$ and $f = f_{VCG}$ for VEGs and VCGs, respectively. (A) The gradients have same first moment M_1 (ie, same v_{enc}) but different durations, which (B) determine the spectral coverage. Inset: secondary peaks in the spectrum with amplitude reduced by a factor of approx. 500 compared to zero frequency amplitude can be neglected. (C) VCG amplitudes are defined by their maximum first moment during encoding time $\max_t M_1(t)$, $t = [0, t_{dur}]$ (see Supporting Information Figure S4). VCGs exhibit a (D) narrow peak in the spectrum that renders them suitable for point-wise probing. VCG, velocity-compensated gradient; VEG, velocity-encoding gradient
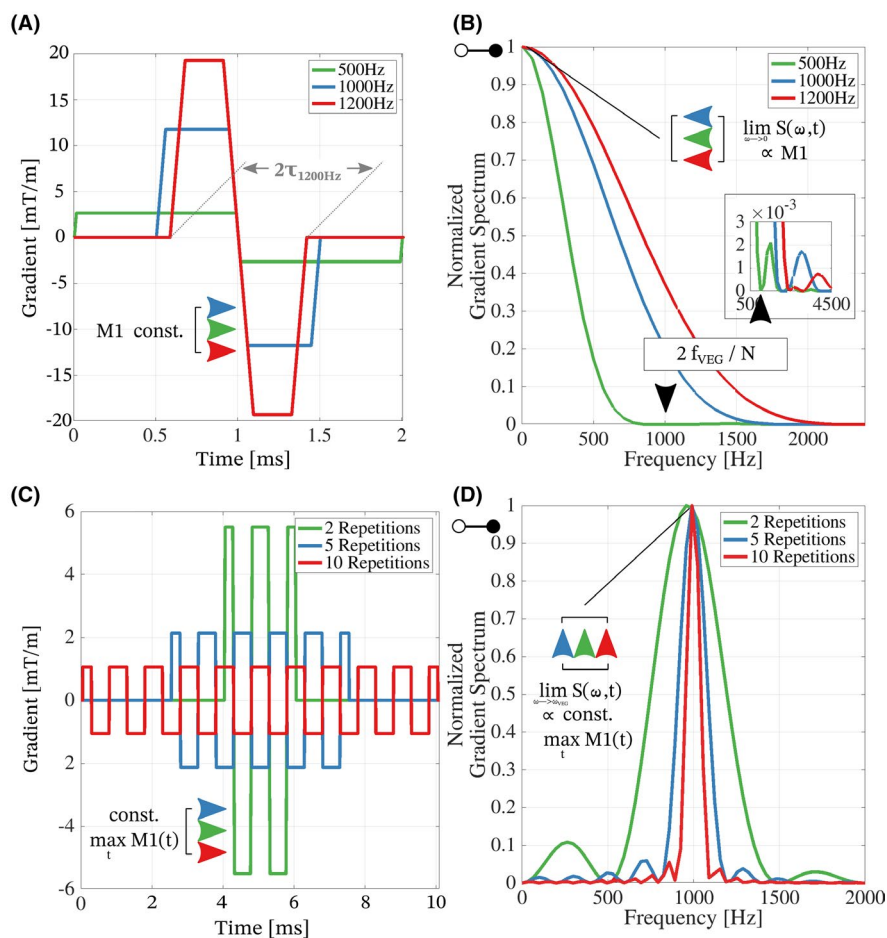
shown. Their amplitude is scaled according to their maximum first moment over time. The VCG spectra $S(\omega, t)$ (Figure 2D) exhibit a lobe at the gradient frequency; however, they do not show a zero-frequency lobe. Their spectra are well suited for point-wise probing the VACF spectrum due to their narrow frequency band in the gradient spectrum.

2.3 | Encoding power of gradients

Given Equation (10), knowledge about both the VACF spectrum $D_{m,n}(\omega)$ and MEG spectrum $S(\omega, t)$ is necessary to estimate the encoding strength $\alpha(t)$. VACF spectra of stenotic flows have been investigated in numerous works.[19,21,38-46] Assuming a simplified 1D model VACF spectrum $E(\kappa, l, c_l)$[35] given by

$$f_l(\kappa, l, c_l) = \left(\frac{\kappa l}{\kappa l + c_l}\right)^{\frac{5}{3}},$$
$$E(\kappa, l, c_l) = \kappa^{-5/3} f_l(\kappa, l, c_l), \tag{16}$$

where κ is the wave number, l a reference length, and $f_l(\kappa, c_l)$ is a nondimensional function which defines the shape of the inertial range and tends to unity for small κl, a VACF spectrum based on $c_l = f_{eddy}^2 l$ can be defined. The cutoff frequency f_{eddy} defines the onset of the $-5/3$ inertial range[35] and ranges from several 10 Hz[42] up to 1000 Hz,[47] depending on the Reynolds number Re and viscosity ν. For example, increasing the viscosity from $\nu_{water} = 0.71 \text{ mm}^2/\text{s}$ to $\nu_{blood} = 2.6 \text{ mm}^2/\text{s}$ at 36°C[48] and keeping other parameters constant increases the eddy frequency almost

fourfold. Exemplary plots of VACF and VEG spectra are depicted in Figure 3A.

Depending on the specific shape of the VACF spectrum, the coverage of the VEG spectrum might be insufficient. Using a normalized form of Equation (10) and $D(\omega) = E(\kappa, l, c_l)$ yields the relative encoding power $\tilde{\alpha}(t)$ of a VEG spectrum $S(\omega, t)$,

$$\tilde{\alpha}(t) = \frac{\int_{-\infty}^{\infty} D(\omega) S(\omega, t) \, d\omega}{\int_{-\infty}^{\infty} D(\omega) \, d\omega}, \tag{17}$$

depending on the eddy frequency, which is shown in Figure 4A, where integration was performed in the frequency range as given in Figure 3. The relative encoding power for a fixed VEG frequency of $f_{VEG} = 900$ Hz but varying f_{eddy} regimes is depicted in Figure 4B.

2.4 | Current approach of intravoxel SD estimation

The IVSD σ is encoded based on the signal model presented by Dyverfeldt et al,[17] which relates the magnitude signal of 2 differently encoded segments $|S(k_{v1})|$ and $|S(k_{v2})|$ using the encoding velocity moments k_{v1} and k_{v2} according to

$$\sigma = \sqrt{\frac{2 \ln\left(\frac{|S(k_{v2})|}{|S(k_{v1})|}\right)}{k_{v1}^2 - k_{v2}^2}}. \tag{18}$$

The model relies on the assumption $\tau_c \gg \tau$, which was estimated around $\tau_c \geq 10 \text{ ms}$[18] based on MRI data.[49] In

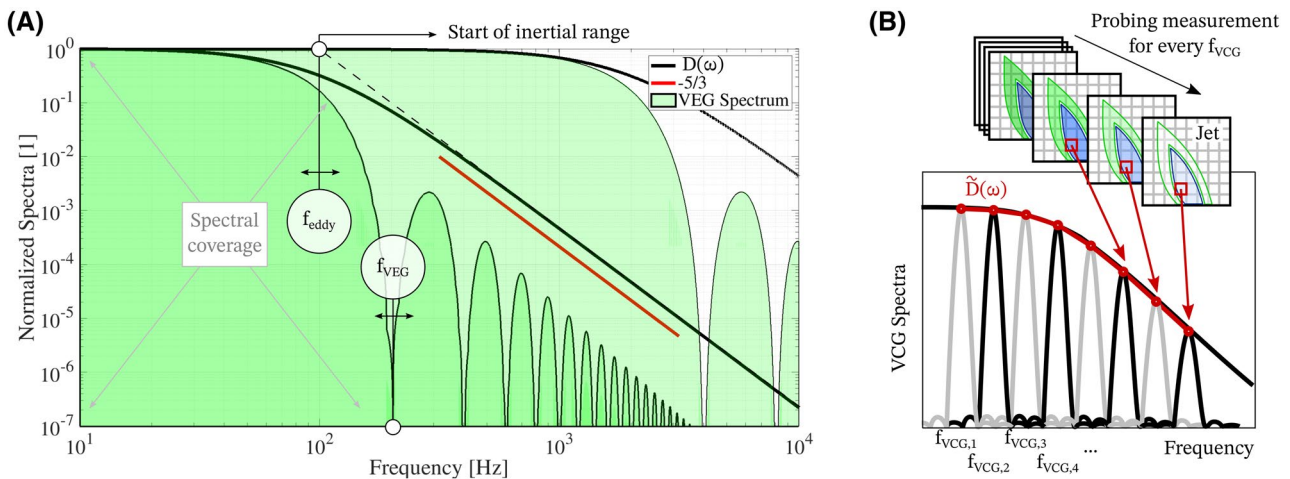**FIGURE 3** (A) Comparison of normalized VACF spectra $D(\omega)$ for $f_{eddy} \in \{100, 2000\}$ Hz and VEG spectra for gradient frequencies $f_{VEG} \in \{100, 2000\}$ Hz using logarithmic scaling. For low-frequency VACF spectra, the high-frequency VEG provide sufficient spectral coverage, whereas the low frequency VEG coverage may be insufficient. $-5/3$ lines depict the slope of the VACF spectra in the inertial range. (B) Using VCG of frequency $f_{VCG,n}$, $n \in \mathbb{N}$, it is possible to reconstruct an estimate $\tilde{D}(\omega)$ of the true VACF spectrum $D(\omega)$ per voxel. This information can be used for correction of limited spectral coverage of VEG. f_{eddy}, eddy frequency; f_{VEG}, VEG frequency
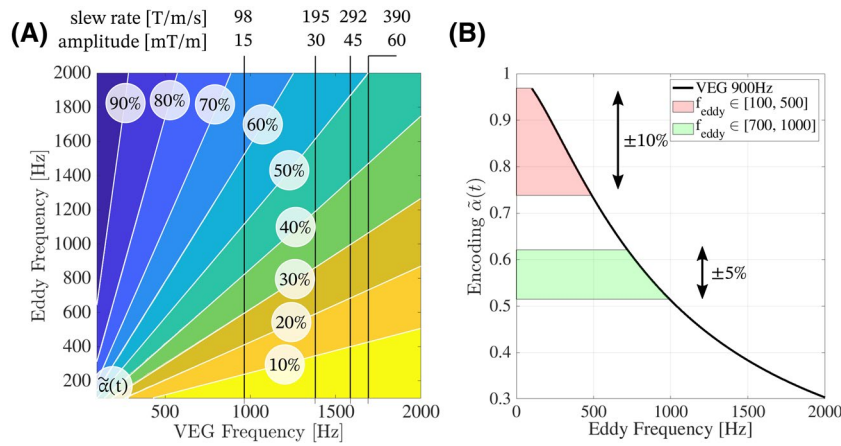
FIGURE 4   (A) Relative encoding power $\tilde{\alpha}(t)$ given by Equation (17) (color and isolines) depending on the f_{VEG} (abscissa) and the f_{eddy} (ordinate) for $v_{enc} = 450$ cm/s for given maximum slew rate and gradient amplitude (respective values stated above the plot). (B) Assuming gradient limits of slew rate 195 T/m/s and maximum gradient amplitude 0.03 T/m (currently available on clinical MRI systems) and VACF spectra comprising $f_{eddy} \in [100, 500]$, for example, the magnitude damping $\exp(\tilde{\alpha}(t))$ of the VEG at maximum frequency 900 Hz varies within up to $\pm 10\%$ depending on f_{eddy} (plot is normalized by value $\tilde{\alpha}(t)$ at first frequency). This results in spatially varying damping and is dependent on the voxel position for inhomogeneous turbulent flows. It cannot be corrected for (all gradients already have same v_{enc}). The uncertainty due to a range of f_{eddy} in a noise-less signal is shown by red/green areas and indicated by percentage values. $\tilde{\alpha}(t)$, relative encoding power

vitro measurement using laser Doppler anemometry of realistic flow conditions and viscosity, predict, however, $\tau_c \approx 1$ ms.[21] This may invalidate the assumption $\tau_c \gg \tau$ as the spectral coverage of the gradients is not taken into account.

3 | METHODS

3.1 | Large eddy simulation

Computational fluid dynamics (CFD) simulations using a large eddy simulation approach in OpenFOAM v1912 were performed on a "stenotic" tube (75% area reduction, cosine shape[50]). A parabolic inlet profile resulting in

$$Re = \frac{uD}{\nu} = 4000, \tag{19}$$

based on the free flow diameter D, the mean flow velocity u at the inlet, and the dynamic viscosity of whole blood at 36°C ($\nu = 2.6$ mm^2/s), was used. Details about the mesh and validation of the CFD solver can be found in Supporting Information Figures S1 and S2, respectively.

For nonstationary input data, as Petersson et al noted,[51] agreement between a large eddy simulation and simulated MRI data is poor if the time-averaged flow quantities are used. Instead of randomly choosing timeframes from the instantaneous solution,[51] the CFD data was extracted continuously in time, beginning at an arbitrary reference time point, and then fed into the MRI simulation. This process

emulates the start of an MRI acquisition at some point in time and running the MRI simulation for the duration of the MEG. Therefore, time-resolved CFD data were exported for slices in the x,z-plane with $\Delta t = 100$ μs and linearly interpolated onto the MRI simulation time grid. Supporting Information Video S1 shows the CFD slices over time.

3.2 | MRI simulation VEG

Our recently presented MRI simulation particle tracing approach[52] was extended to include random motion based on a discrete random walk model.[53] The fluctuating velocities v'_x, v'_z were kept constant for a spatially varying time constant defined by the Lagrangian integral time

$$T_L \approx 0.30 \frac{k}{\varepsilon} = 0.30 \frac{1}{\omega}, \tag{20}$$

where k, ε, and ω denote the TKE; the standard dissipation rate; and the specific dissipation rate of TKE of the large eddy simulation turbulence model, respectively. The eddy lifetime $\tau_{eddy} = 2T_L$ relates to the eddy frequency as $f_{eddy} = 1/\tau_{eddy}$. As shown in Figure 5, the eddy frequency of the dataset used as input data was in the range $f_{eddy} = [1000, 5000]$Hz. A similar approach has also been used in other works concerned with turbulent MRI simulations.[54] The current simulation does not assume isotropy and employs Cholesky decomposition to draw samples from correlated distributions given by the covariance matrix Σ according to
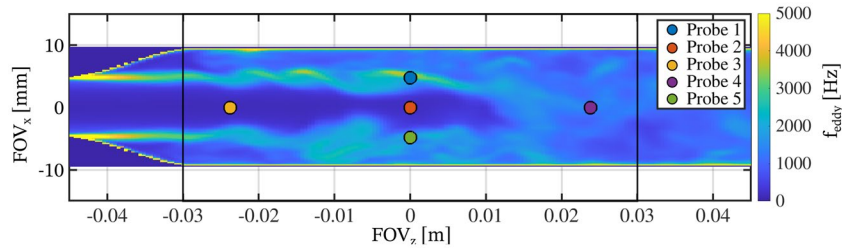
FIGURE 5 Probe positions P1 to P5 used for the Lagrangian VACF and VACF spectrum calculation. Underlay image encodes the f_{eddy} (colorbar) of the first CFD input data frame. Probe 1 and 5 are in high eddy frequency regions (jet border), whereas probe 2 and 3 are in low eddy frequency regions (jet core). Probe 4 is set in an intermediate f_{eddy} region (transitional region where the jet breaks down). Markers not to scale with the probe radius r. CFD, computional flow; Pi, Probe i

$$\zeta_{x,z} \sim \mathcal{N}(0,1),$$
$$LL^T = \Sigma, \quad \Sigma = \begin{bmatrix} \sigma_{xx}^2 & \sigma_{xz}^2 \\ \sigma_{zx}^2 & \sigma_{zz}^2 \end{bmatrix}, \quad \Sigma \text{ is spd,} \qquad (21)$$
$$\begin{bmatrix} v_x' \\ v_z' \end{bmatrix} = L \begin{bmatrix} \zeta_x \\ \zeta_z \end{bmatrix},$$

where Σ is derived from RST values σ_{mn}^2, $m, n \in \{x, z\}$ taken from CFD data.

The computational framework,[52] written in MatLab R2017b (MathWorks, Natick, MA), was modified to utilize GPU functions, and the forward Euler method (fixed step length of $\Delta t = 1\,\mu s$) was used to increase speed and extensibility. A total of $n_{tot} = 10^6$ tracer particles were seeded in the simulated FOV. The particles' position increment per time step is given by $\Delta i(t + \Delta t) = (\bar{v}_i(t) + v_i'(t))\, \Delta t$, $i \in \{x, z\}$. The CFD input time frames were linearly interpolated in time between simulation time steps t and $t + \Delta t$. Supporting Information Video S2 exemplary shows the particle motion over simulation time.

Simulation runs with different gradient frequencies f_{VEG} (ie, several $S(k_{v2})$, same v_{enc}) were compared to a nonencoded reference data ($S(k_{v1})$, that is, without applying a VEG and hence $v_{enc} = \infty$). The segments $v_{enc} \neq 0$ and $v_{enc} = \infty$ (reference) were not assumed to be separated in time, that is, using the same CFD input data time frames. This mimics a beat-interleaving strategy of motion-encoding segments as in cardiac-gated scans. The encoding was simulated only in z-direction because the extension to other directions is readily made and provides no new insights. Equation (18) was used for calculation of σ_{zz}. Ground truth was assumed to be the first CFD input data time frame at $t = 0$ down-sampled to the MRI image size.

To keep the simulation tractable on a normal workstation, the simulation time was limited to the velocity-encoding phase t_{dur}, where $t_{dur} = \frac{1}{\min(f_{VEG})} = 2\,ms$ because $f_{VEG} = \{500, 1000, 1200\}\,Hz$. Of note, this mimics

instantaneous readout at time t_{dur}, which enables the current work to focus on the effects of motion encoding rather than readout artefacts due to motion.[52] No noise or coil sensitivities were simulated. In addition, particles were seeded on a 2D plane, and through-plane velocities were neglected to reduce computational load. The simulation was repeated 10 times, and resulting images were averaged.

3.3 | Gradient waveform spectra

The VEG spectrum $S(\omega, t)$ (Equation (11)) was evaluated after the gradient was played out, that is, at $t = t_{dur}$. The VEG waveforms used in the simulation are depicted in Figure 2A. The gradient waveforms were centered around $t_{dur}/2$. The VEG spectra depicted in Figure 2B were normalized to their maximum value, which is proportional to their first gradient moment.[26]

3.4 | Intravoxel mean velocity variations

The estimation of Intravoxel mean velocity variations as given by Dyverfeldt[18] reads

$$\sigma_{turb} = \sqrt{\sigma_{IVSD}^2 - \frac{2}{k_v^2} \ln\left(\frac{|S_{MVV}(0)|}{|S_{MVV}(k_v)|}\right)}, \qquad (22)$$

where σ_{turb} and σ_{IVSD} denote the IVSD due to turbulence and the measured IVSD, respectively. Estimation of the term inside the brackets is based on a linear velocity gradient across a voxel.[18] This estimation is valid as long as magnetization does not move across several voxels during motion encoding. Because the current paper is concerned with high-flow regimes, it is estimated that, for severe stenosis ($v_{max} \geq 4\,m/s^6$) and typical motion-encoding durations

(0.5-1 ms), magnetization moves by more than 1 voxel (typical resolution 2.5 mm) in the jet region.

The IVSD due to mean velocity only is given as

$$\sigma_{MVV}^2 = \frac{2}{k_v^2} \ln\left(\frac{|S_{MVV}(0)|}{|S_{MVV}(k_v)|}\right), \tag{23}$$

and can be assessed by performing the simulation without fluctuating velocities. Because massless tracer particles are used, any spatial gradient in the mean velocity field will contribute to σ_{MVV}^2 (see Appendix; particle motion equation). For correction, σ_{MVV}^2 is subtracted from σ_{IVSD}^2 to obtain results devoid of IVSD due to mean velocity. Resulting IVSD from mean velocity σ_{MVV} is presented in Supporting Information Figure S3.

3.5 | VACF and VACF spectrum $D(\omega)$

The Lagrangian velocity autocorrelation function VACF is given by calculating the autocorrelation of velocity samples of probe velocities. The particles were selected at $t = 0$ at given locations shown in Figure 5 within a radius of $r = 1$ mm,

$$VACF_{m,m,p}(t_s) = \langle u_{m,p}(r_s, t_s)\, u_{m,p}(r_s, t_s)\rangle, \; m \in \{x, z\}, \tag{24}$$

where r_s, t_s denote the probe position and probed time, respectively, and $p \in \{particle\, indices\, within\, r\}$. Taking the mean $VACF_{m,m}(t_s) = \frac{1}{|p|} \sum_{p'=1}^{|p|} VACF_{m,m,p'}(t_s)$, multiplying it with a Tuckey window of the same length and applying the discrete Fourier transform results in the velocity autocorrelation spectrum (VACF spectrum) $D_{m,m}(\omega)$.

3.6 | MRI simulation VCG

For probing the VACF spectrum, the MRI simulation was conducted assuming a high-performance gradient system (maximum gradient amplitude 80 mT/m, maximum slew rate 210 T/m/s); gradient frequencies were set to $f_{VCG} = [100, 200, \cdots, 5000]$Hz, resulting in 50 probing frequencies; and waveforms were repeated for

$$N_{f_{VCG}} = 2\left\lfloor \frac{f_{VCG}}{\max(f_{VCG})} \right\rfloor \tag{25}$$

to achieve approximately the same spectral band width. Given a fixed-time encoding window $t_{dur} = \min(N_{f_{VCG}})/\min(f_{VCG}) = 20$ ms and $N_{f_{VCG}}$ repetitions for VCG of frequency f_{VCG}, the spectral width of the

response lobe becomes independent of f_{VCG}, allowing the entire spectrum to be probed by changing the gradient frequency. VCG waveforms were calculated such that their maximum first moment $M_{1,\max} = \max_t (M_1(t)) = \int_{t_0}^{t_0+t} G(t)(t - t_0)\, dt$ corresponded to $v_{enc} = \pi/(\gamma M_{1,\max}) = 450$ cm/s (see Supporting Information Figure S4), where again $t_0 = 0$ was assumed.

Resulting gradient spectra and waveforms are depicted in Figure 9C,D, respectively. Due to integer rounding in Equation (25), the relationship between first moment and peak values in the spectra holds only approximatively. The resulting images were calculated according to Equation (18), where σ_{zz} denotes the encoding of the intravoxel SD along the direction z.

For probing the VACF spectrum, mean velocities were set to zero to avoid changes in turbulence parameters due to mean particle motion and to enable comparison to ground truth. Because particles are expected to stay within a region with spatially homogeneous parameters, Lagrangian (moving particles) and Eulerian (voxel) spectra yield the same result. To ensure spatial and temporal homogeneity, $f_{eddy} = 1$ kHz and $\sigma_{zz} = 0.3$ m/s were fixed for all CFD input data time frames for all voxels.

3.7 | Spectral correction method

By employing knowledge about the spectrum $D(\omega)$ and the gradient spectrum $S(\omega, t)$, the limited spectral-encoding ability of the VEG gradients was corrected on a voxel basis. For given flow, this results in a quantitative correct estimate of SDs σ_{mn}, $m, n \in \{x, y, z\}$.

The per-voxel estimate of VACF spectra $\tilde{D}(\omega)$ was calculated from simulations with VCGs by linearly interpolating between probed frequencies (Figure 3B). The relative encoding power $\tilde{\alpha}(t)$ per voxel was given by the full version of Equation (17) and used for correction by employing

$$\sigma_{corrected} = \sigma_{f_{VEG}} / \tilde{\alpha}_{f_{VEG}}, \tag{26}$$

given an uncorrected measurement of $\sigma_{f_{VEG}}$ resulting in the corrected estimate $\sigma_{corrected}$ of IVSD for a given VEG frequency f_{VEG} using Equation (18).

Without additional VCG measurements, the VEG spectrum $S(\omega, t)$ could be estimated from gradient waveforms exclusively. Assuming $D(\omega) \approx$ const. $\forall \omega$, Equation (17) resulted in an estimate for the encoding power for a given VEG

$$\tilde{\alpha}_{f_{VEG}}(t) = \int_{-\infty}^{\infty} S(\omega, t)\, d\omega, \tag{27}$$

which was used to correct for experiments employing VEGs. Phase-contrast sequences with high and low v_{enc} values to account for nonlinearities in Equation (18) may result in different VEG frequencies and, if uncorrected for, inconsistencies in σ_{mn} estimation across v_{enc} values.[55] The spectra $S(\omega, t)$ of VEGs $f_{VEG} = \{500, 1000, 1200\}$ Hz were calculated according to Equation (11), and the encoding power across v_{enc} values was normalized using

$$\widetilde{\alpha}'_{f_{VEG}} = \frac{\widetilde{\alpha}_{f_{VEG}}}{\widetilde{\alpha}_{\max(f_{VEG})}}. \tag{28}$$

4 | RESULTS

4.1 | VACF spectrum

The VACFs in x and z direction and their spectra at different probe positions are depicted in Figure 6. Depending on the specific probe position r_s as a function of time and corresponding $f_{eddy}(r_s, t)$, the VACF spectrum follows the shape of exemplary model spectra defined in Equation (16) with the roll-off frequency related to the eddy frequency. The spectrum is inherently multiplied by a sinc function due to the discrete random walk model used; the local minima are given by the update rate f_{eddy} the

magnetization experiences during simulation time. Due to the high flow velocity in z direction (Figure 6C,D), it can be seen that probe 1 has a low correlation during $t = [0, 0.1]$ ms because the probed particles start in a high f_{eddy} region and are transported to a lower f_{eddy} region. This results in reduced correlation due to spatial inhomogeneity of velocity and turbulence parameters, and subsequently a higher frequency coverage in the spectrum.

4.2 | Mean velocity and turbulence parameter estimation

In the plots shown in Figure 7, results of estimated mean velocities are similar for different VEG frequencies. Spatial misregistration due to finite VEG duration is found when compared to ground truth. The spatial misregistration corresponds to the distance $\Delta z = V_z \tau$ that a particle would move during time $t_{dur}/2$, because VEGs are centered at $t_{dur}/2$. The misregistration is given by $\Delta z = 2$ mm in a region where the mean velocity is approximately 2 m/s and $t_{dur} = 2$ ms. For the IVSD results depicted in Figure 8, σ_{zz} is seen to be reduced by 50% when compared to ground truth when using a VEG of 500 Hz. On the other hand, increasing the VEG frequency decreases the difference between σ_{zz} and ground
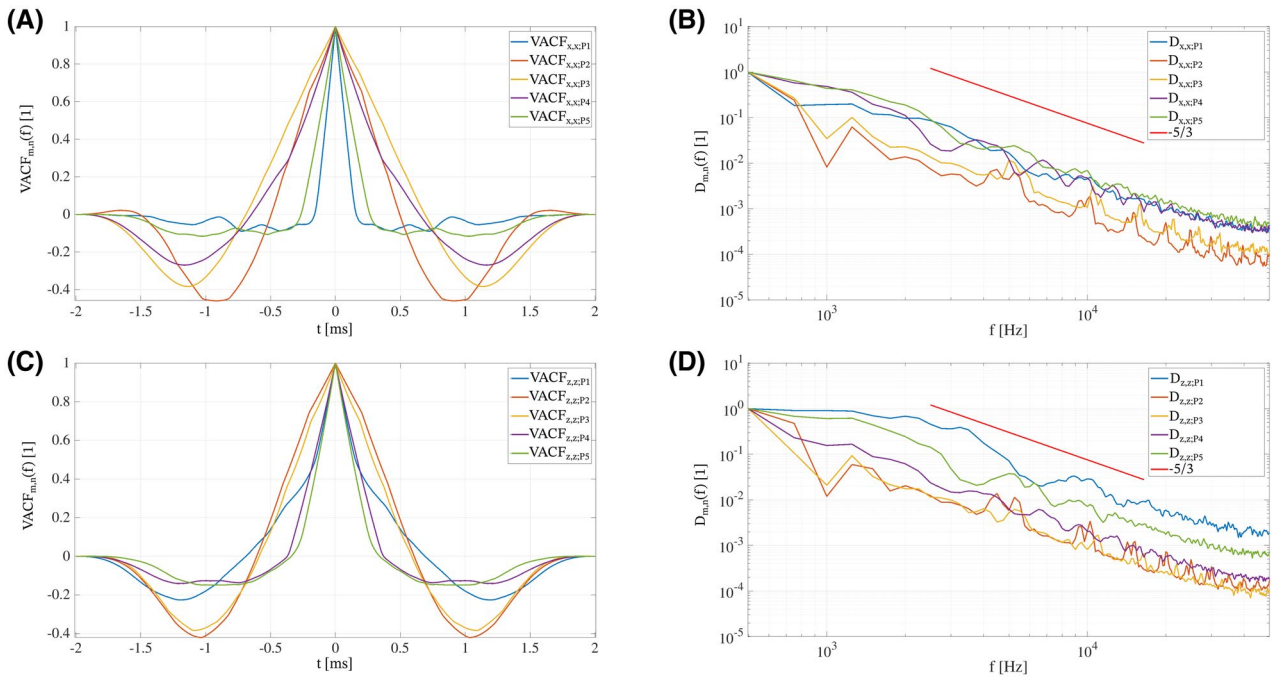

FIGURE 6 Lagrangian VACF in (A) x direction (index xx) and (B) z direction (index zz) for different probe positions P1 to P5. (B), (D): VACF spectra in x and z direction. Different probe positions relate to regions of different eddy frequencies and therefore different autocorrelation functions and spectra. Particles in regions of high f_{eddy} show fast decaying VACFs (eg, probe 1, 2). Transport to a different region due to mean flow results in a kink in the VACF (eg, VACF in z direction probe 1). Highest frequency of start of the inertial range in (D) (stream-wise) is found at 2 kHz for probe 1
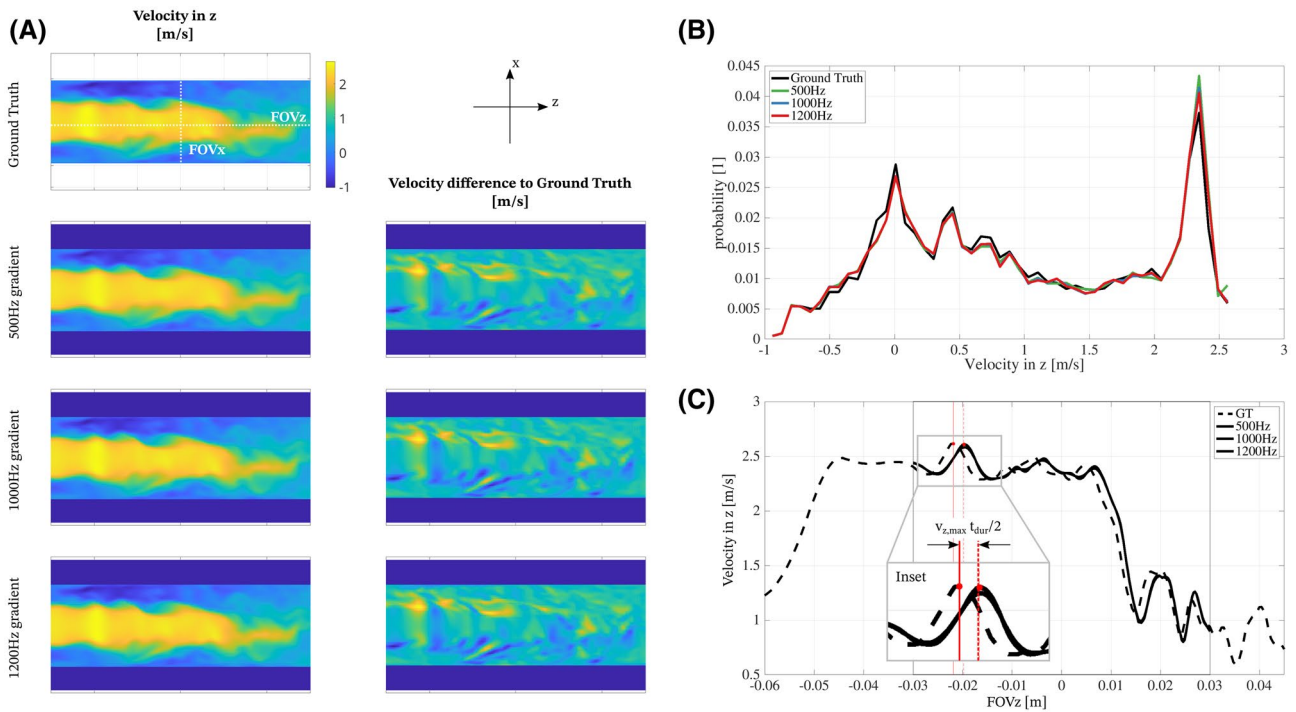
FIGURE 7   (A) Comparison of velocity simulation output for f_{VEG} = {500, 1000, 1200} Hz to ground truth yields that the mean velocity is found to be imaged correctly and results in comparable images for different f_{VEG}. (B) The mean velocity distribution does not depend on f_{VEG}. (C) The mean velocity profile shows only spatial misregistration artefacts compared to ground truth, which relates to $v_{z,max} t_{dur}/2$ because instantaneous imaging is assumed at the end of the VEG (inset)
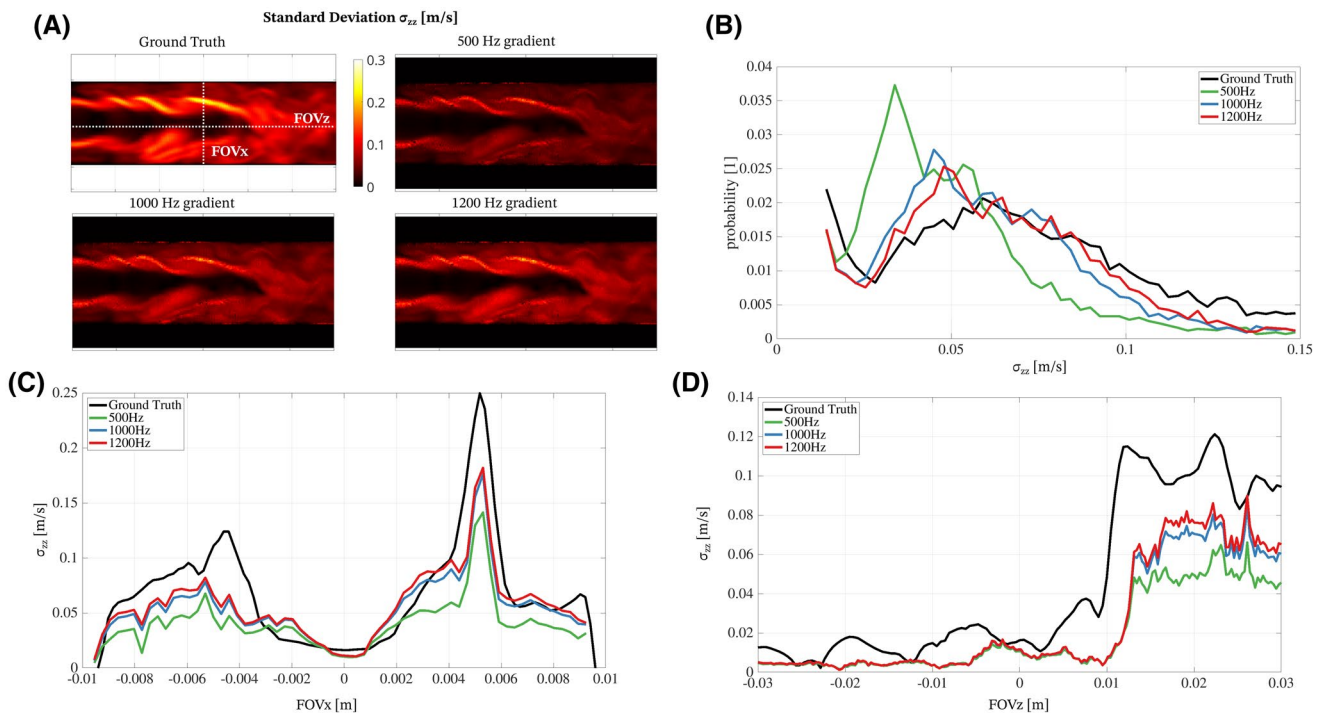

FIGURE 8   Comparison of SD σ_{zz} for f_{VEG} = {500, 1000, 1200} Hz in z direction with GT shows that σ_{zz} is systematically underestimated and its estimated values differ for different f_{VEG}. (A) Increasing f_{VEG} results in an improved estimation of σ_{zz} compared to ground truth. (B) The σ_{zz} distribution is shifted toward lower values as f_{VEG} decreases. This results in increased underestimation of SD values for decreased f_{VEG}. σ_{zz} profiles are depicted along FOV$_x$ (C) and FOV$_z$ (D). Level of underestimation compared to GT is increased in regions of high eddy frequency (compare Figure 5). Due to mean velocities, misregistration artefacts are found in (D) (compare also Figure 7). GT, ground truth

truth. Using histogram analysis in Figure 8B, a difference of mean value of 29% between 500 and 1200 Hz gradient is found, whereas mean velocity distributions show no difference. Of note, the model by Dyverfeldt[18] would predict the same values of σ_{zz} for all tested VEG frequencies because of the same v_{enc} used.

4.3 | Mean flow influence on turbulence estimation

Conducting the simulation without random motion components $\begin{bmatrix} x' \\ z' \end{bmatrix}$ in Equation (21) results in an estimate of σ_{zz} due to mean velocity only. Resulting σ_{zz} plots and their respective histograms can be found in Supporting Information Figure S3. Given massless tracer particles were assumed, the imaged σ_{zz} due to mean velocity only corresponds to the mean velocity gradient in VEG direction and is not dependent on the VEG frequency. Tracer particle dynamics are further discussed in the Appendix.

4.4 | Corrected turbulence estimation

In Figure 9A, good agreement is found between normalized VACF spectra given by Lagrangian probes and the VACF spectrum estimated from VCG probing measurements, therefore confirming the feasibility of probing the VACF spectra. Using the correction method employing knowledge about both the VEG spectra and the probed VACF spectra using VCG measurements, Figure 9B shows that the estimation error reduces from −49% to −10% for f_{VEG} = 500 Hz and from −21% to −5% for f_{VEG} = 1200 Hz. Figure 9C and D show spectra and waveforms of VCGs with varying frequencies used in the probing measurement. Due to their narrow bandwidth of approx. 100 Hz, point-wise probing of the VACF spectrum is possible.

In Figure 10, estimates of IVSD are presented that have been corrected without additional probing but by employing Equation (28). The IVSD estimates are coherent across different values of v_{enc} but underestimate ground truth. This is confirmed in the histogram analysis in Figure 10B and profiles in Figure 10C and D.
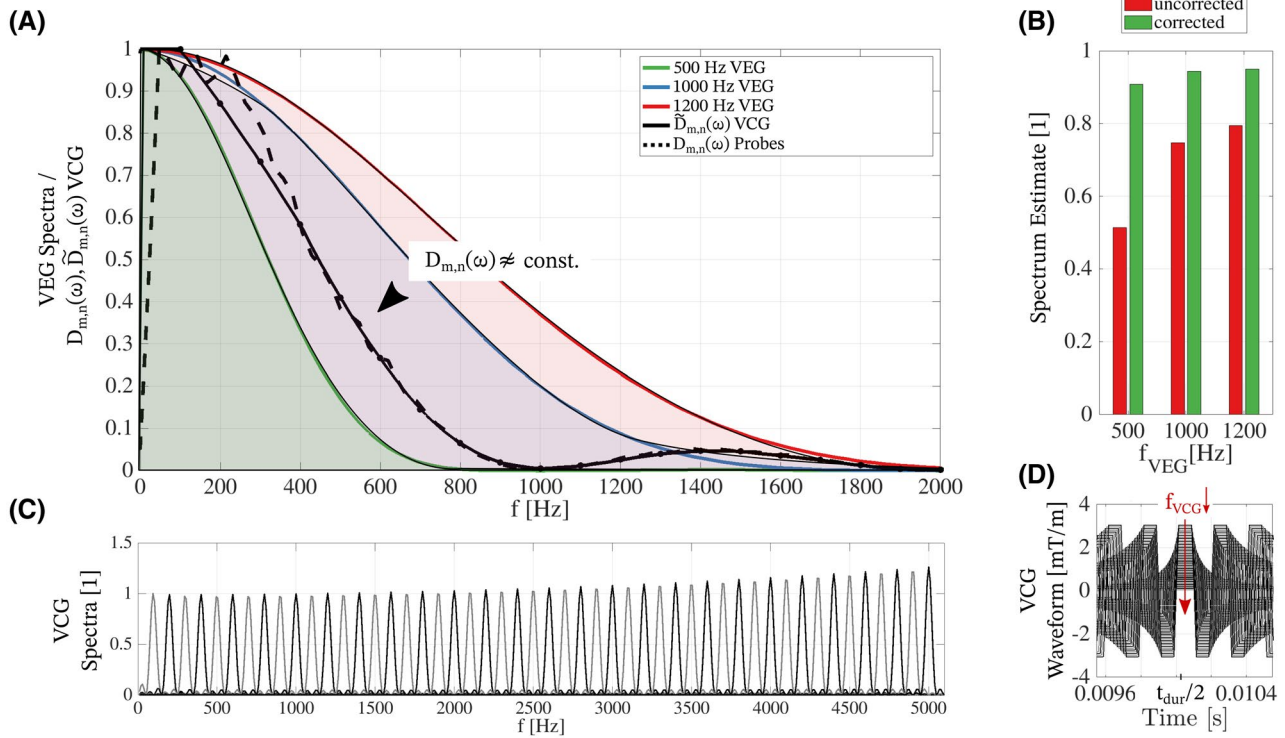

FIGURE 9 (A) Estimated VACF spectrum $\tilde{D}_{m,n}(\omega)$ (black continuous line) compared to VACF spectra $D_{m,n}(\omega)$ (black dotted line) using spatially invariant input data and zero mean velocity to enable direct comparison. Each point of the continuous curve relates to a simulation run with the respective VCG. Good agreement between the Lagrangian VACF spectrum and the estimated spectrum is found. (B) Applying the correction method employing both $\tilde{D}_{m,n}(\omega)$ (estimated from VCG measurements) and $S(\omega)$ (calculated from VEG parameters), the underestimation is reduced from 49% to 10% for 500 Hz VEG. (C) Normalized spectra of VCGs used for probing the VACF spectrum. Due to integer rounding in Equation (25), different numbers of repetitions may result in differences in spectral bandwidth. Spectra are normalized in the plot by the initial probing gradient where, due to slew rate limitations, maximum spectra values increase for higher frequencies. (D) VCG waveforms used for probing. The plot depicts details of the full waveforms for $t = [0, t_{dur}]$
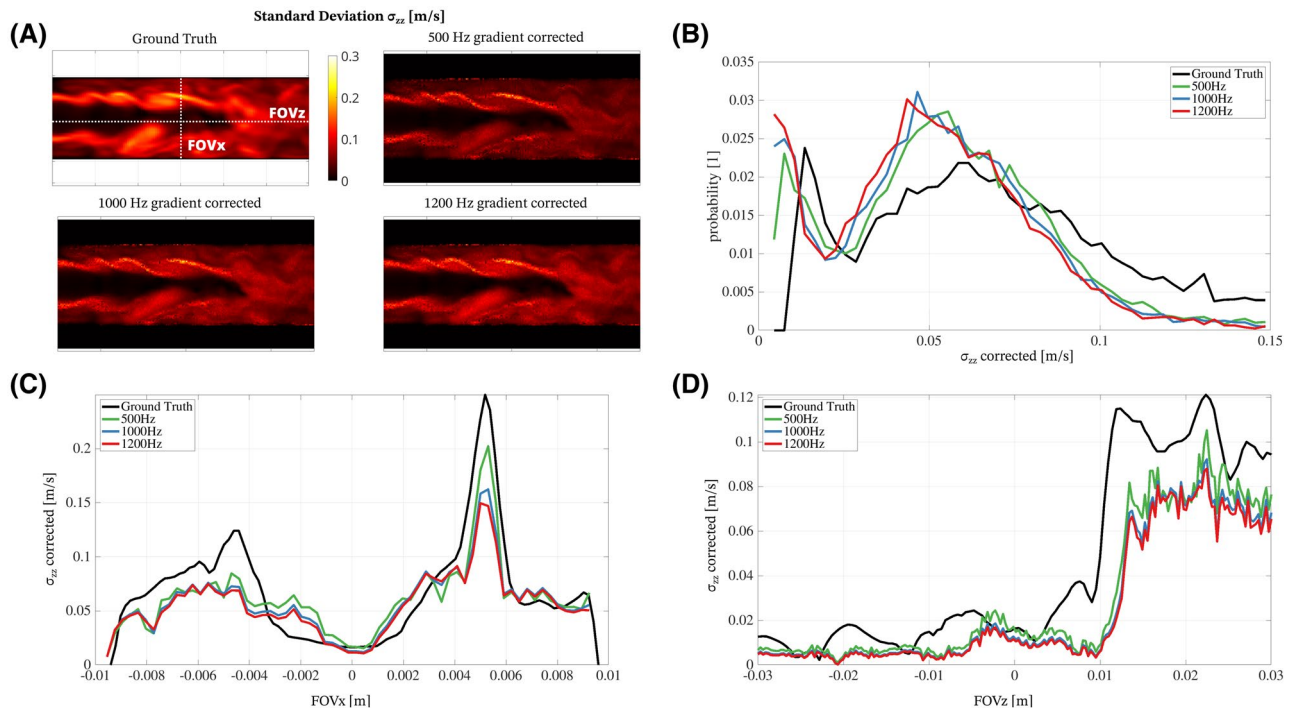
FIGURE 10 (A) Estimated SD σ_{zz} for VEG frequencies $f_{VEG} = \{500, 1000, 1200\}$Hz with applied VEG spectrum correction according to Equation (28) without prior probing of the VACF spectrum by VCG measurements. (B) The σ_{zz} distribution is consistent within different f_{VEG}. Compared to ground truth, the distribution is underestimated because $\max(f_{VEG}) < \infty$. σ_{zz} profiles along FOV_x (C) and FOV_z (D) show coherent estimates of the SD across different f_{VEG} after applying the correction method

5 | DISCUSSION

Based on the framework presented, VEG and their spectral response in relation to probing turbulent flow have been investigated.

Assuming velocity autocorrelation function spectra of turbulent flow,[35] and VEG gradients with a v_{enc} of 450 cm/s and 1 ms duration, current models for turbulence quantification[18] are shown to systematically underestimate turbulence parameters given a typical image resolution of 2.5 mm. In addition, depending on position in the turbulent region, the degree of underestimation varies with the VEG frequency. Higher VEG frequencies are shown to reduce the underestimation. At the maximum frequency given by the maximum slew rate and gradient strength available on clinical MRI systems, significant underestimation of turbulence parameters remained. Increasing the voxel size, however, is expected to counteract this effect and may even result in overestimation of turbulence parameters.[56] Estimation of the mean velocity was not affected, aside from misregistration errors due to finite time duration of the VEG.

Current turbulence quantification models[18] assume that the Lagrangian correlation time scale is much longer than the time duration of the VEG. In the current paper, based on CFD simulations assuming realistic flow regimes and viscosity, the first zero crossing of the VACF was

found before 1 ms, which relates to correlation time scales shorter than typical VEG durations. In vitro experiments using a blood fluid analog report the first zero crossing around 3 ms,[21] depending on the temporal phase of the pulsatile flow and the position upstream of their artificial aortic valve. Other in vitro[57] and in vivo[43] works report significant energy density above 500 Hz in their spectra.

On current MRI systems, the v_{enc} value is set by the user, whereas gradient timings are optimized depending on other sequence parameters. Because the spectral response depends on the VEG duration, such an approach does not provide full control for quantifying turbulence parameters. For VEG of 900 Hz ($t_{dur} \approx 1\,\text{ms}$), it was found that the turbulence parameter estimation uncertainty for a range of VACF spectra can exceed $\pm 10\%$ in addition to the systematic, quantitative underestimation of turbulence parameters.

It is important to note that, depending on the duration of the VEG, estimation of turbulence parameter results in different values. This effect is not dependent on v_{enc} and cannot be completely corrected for without information of both the VEG spectrum and the velocity autocorrelation function (VACF) spectrum.

To address systematic underestimation of turbulence parameters using VEGs, a method using velocity-compensated waveforms has been presented. VCGs exhibit

a narrow peak in the gradient spectrum and hence are suitable for encoding and reconstructing the VACF spectrum with improved accuracy. Comparison to spectra of simulated probes yielded very good agreement. Because VACF spectra vary spatially in turbulent flows,[39] the presented method holds potential to correct for systematic errors in turbulence quantification on a voxel basis.

To ensure applicability of the correction method in practice without the need for additional measurements, the possibility of correction using only VEG spectra without probing the VACF spectrum was investigated. It was found that the RST estimates could be corrected to be coherent throughout different VEG frequencies.

5.1 | Limitations

The current work is limited in terms of its restriction to nonpulsatile flow boundary conditions in the CFD simulation. However, because the MRI simulation concerned with VEGs focuses on the velocity-encoding time span ($t_{dur} \leq 2$ ms), realistic aortic inlet conditions would only result in negligible changes of flow rate during t_{dur}.[58] Of note, the VEG MRI simulation itself employs time-varying input data from CFD. The 2D MRI simulation with input data from 3D CFD does not consider through-plane velocities. Nevertheless, because the evaluation only included in-plane parameters, no effects on the results are to be expected. No noise or coil sensitivities were simulated. Due to limited slew rates, depending on their frequency, VEGs or VCGs may have small gradient amplitudes that hamper the applicability in a real experiment due to the presence of noise. In vitro experiments and optimized waveforms[59] will be subject to future research. Whereas the VCG waveforms used in this work respected gradient slew rate/amplitude limits of available MRI gradient systems, they employed increased encoding times ($t_{dur} = 20$ ms). Accordingly, TEs are long, leading to reduced SNR due to T_2^* decay. Practical investigation of SNR-related limitations of turbulent flow encoding using VCGs are planned for our future research.

The reference segment $v_{enc} = \infty$ and encoded segments $v_{enc} \neq 0$ have not been separated in time during the simulation process. Because readout effects were the focus of another work[52] and have not been considered, no signal attenuation and phase accumulation result for $v_{enc} = \infty$, rendering the reference segment start time independent. If readout effects were to be considered, particle tracing must be performed for $v_{enc} = \infty$ and $v_{enc} \neq 0$ segments separately, and input data time frames must be separated based on the assumed interleaving strategy of the MRI sequence.

Assumptions about the VACF spectra are based on CFD results using realistic flow parameters; however, the VACF spectrum may differ from the simulated spectra in reality. The probing of VACF spectra in vitro will be a subject of future research. Previous works[54] employed a similar particle tracing approach but did not provide any information about VACF spectra. The current work is employing a discrete random walk model; however, alternatives such as continuous random walk models could be used.[60] In addition, altering the viscosity of the working fluid changes the VACF spectrum, which hampers comparability of different works. In this work, the viscosity of whole blood and a realistic Reynolds number were used, intended to mimic in vivo flow parameters.

Relying on a particle-tracing approach, particles' dynamics influence the simulation results. Rather than imposing specific particle parameters (eg, particle drag force outlined in Equation (46)), massless particles were used. These particles do not suppress any dynamics that might be important for tracing, however; they are susceptible to gradients of the mean velocity field. To overcome this limitation, mean velocity variation correction was applied (Supporting Information Figure S3).

6 | CONCLUSION

Theoretical considerations and computer simulations as presented in this work suggest that bipolar VEGs in phase-contrast MRI of stenotic flows with short correlation times result in systematic and significant underestimation of turbulence parameters. To address this shortcoming, tailored VCGs are proposed to offer an approach to improved quantitative mapping of turbulent blood flow characteristics.

DATA AVAILABILITY STATEMENT

The CFD simulation source files included output data and MRI simulation MatLab R2020a (MathWorks) scripts have been uploaded to Open Science Framework and can be found at https://osf.io/ebdga/ (10.17605/OSF.IO/EBDGA).

ORCID

Hannes Dillinger https://orcid.org/0000-0002-5597-5273
Charles McGrath https://orcid.org/0000-0002-3110-4051
Christian Guenthner https://orcid.org/0000-0001-8707-7016
Sebastian Kozerke https://orcid.org/0000-0003-3725-8884

REFERENCES

1. Dyverfeldt P, Bissell M, Barker AJ, et al. 4D flow cardiovascular magnetic resonance consensus statement. *J Cardiovasc Magn Reson*. 2015;17:72.

2. Hsiao A, Tariq U, Alley MT, Lustig M, Vasanawala SS. Inlet and outlet valve flow and regurgitant volume may be directly and reliably quantified with accelerated, volumetric phase-contrast MRI. *J Magn Reson Imaging*. 2015;41:376-385.

3. Mahadevia R, Barker AJ, Schnell S, et al. Bicuspid aortic cusp fusion morphology alters aortic three-dimensional outflow patterns, wall shear stress, and expression of aortopathy. *Circulation*. 2014;129:673-682.

4. François CJ, Markl M, Schiebler ML, et al. Four-dimensional, flow-sensitive magnetic resonance imaging of blood flow patterns in thoracic aortic dissections. *J Thorac Cardiovasc Surg*. 2013;145:1359-1366.

5. Chen SSM, Kilner PJ. Unilateral pulmonary artery branch stenosis: diastolic prolongation of forward flow appears to maintain flow to the affected lung if the pulmonary valve is competent. *Int J Cardiol*. 2013;168:3698-3703.

6. Baumgartner H, Falk V, Bax JJ, et al. 2017 ESC/EACTS Guidelines for the management of valvular heart disease. *Eur Heart J*. 2017;38:2739-2786.

7. Binter C, Gotschy A, Sündermann SH, et al. Turbulent kinetic energy assessed by multipoint 4-dimensional flow magnetic resonance imaging provides additional information relative to echocardiography for the determination of aortic stenosis severity. *Circ Cardiovasc Imaging*. 2017;10:e005486.

8. Walheim J, Dillinger H, Kozerke S. Multipoint 5D flow cardiovascular magnetic resonance—accelerated cardiac- and respiratory-motion resolved mapping of mean and turbulent velocities. *J Cardiovasc Magn Reson*. 2019;21:42.

9. Walheim J, Dillinger H, Gotschy A, Kozerke S. 5D flow tensor MRI to efficiently map Reynolds stresses of aortic blood flow in-vivo. *Sci Rep*. 2019;9:18794.

10. Ha H, Kvitting JPE, Dyverfeldt P, Ebbers T. Validation of pressure drop assessment using 4D flow MRI-based turbulence production in various shapes of aortic stenoses. *Magn Reson Med*. 2019;81:893-906.

11. Kuethe DO, Gao JH. NMR signal loss from turbulence: models of time dependence compared with data. *Phys Rev E*. 1995;51:3252-3262.

12. Kuethe DO. Measuring distributions of diffusivity in turbulent fluids with magnetic-resonance imaging. *Phys Rev A*. 1989;40:4542-4551.

13. Gao J-H, Gore JC. Turbulent flow effects on NMR imaging: measurement of turbulent intensity. *Med Phys*. 1991;18:1045-1051.

14. Gatenby JC, Gore JC. Mapping of turbulent intensity by magnetic resonance imaging. *J Magn Reson B*. 1994;104:119-126.

15. Gatenby JC, Gore JC. Characterization of turbulent flows by NMR measurements with pulsed gradients. *J Magn Reson A*. 1994;110:26-32.

16. Gatenby JC, Gore JC. Echo-planar-imaging studies of turbulent flow. *J Magn Reson A*. 1996;121:193-200.

17. Dyverfeldt P, Sigfridsson A, Kvitting JPE, Ebbers T. Quantification of intravoxel velocity standard deviation and turbulence intensity by generalizing phase-contrast MRI. *Magn Reson Med*. 2006;56:850-858.

18. Dyverfeldt P, Gårdhagen R, Sigfridsson A, Karlsson M, Ebbers T. On MRI turbulence quantification. *Magn Reson Imaging*. 2009;27:913-922.

19. Clark C. Turbulent velocity measurements in a model of aortic stenosis. *J Biomech*. 1976;9:677-687.

20. Clark C. Turbulent wall pressure measurements in a model of aortic stenosis. *J Biomech*. 1977;10:461-472.

21. Liu JS, Lu PC, Chu SH. Turbulence characteristics downstream of bileaflet aortic valve prostheses. *J Biomech Eng*. 2000;122:118-124.

22. Stepišnik J. Analysis of NMR self-diffusion measurements by a density matrix calculation. *Phys Rev B Condens Matter*. 1981;104:350-364.

23. Stepišnik J. Measuring and imaging of flow by NMR. *Prog Nucl Magn Reson Spectrosc*. 1985;17:187-209.

24. Callaghan PT, Stepišnik J. Frequency-domain analysis of spin motion using modulated-gradient NMR. *J Magn Reson Ser A*. 1995;117:118-122.

25. Newling B, Poirier CC, Zhi Y, et al. Velocity imaging of highly turbulent gas flow. *Phys Rev Lett*. 2004;93:154503.

26. Callaghan PT. *Principles of Nuclear Magnetic Resonance Microscopy*. Oxford, UK: Clarendon Press; 1991.

27. Kubo R. Generalized cumulant expansion method. *J Phys Soc Japan*. 1962;17:1100-1120.

28. Ning L, Setsompop K, Westin CF, Rathi Y. New insights about time-varying diffusivity and its estimation from diffusion MRI. *Magn Reson Med*. 2017;78:763-774.

29. Ha H, Lantz J, Haraldsson H, et al. Assessment of turbulent viscous stress using ICOSA 4D flow MRI for prediction of hemodynamic blood damage. *Sci Rep*. 2016;6:39773.

30. Caprihan A, Seymour JD. Correlation time and diffusion coefficient imaging: application to a granular flow system. *J Magn Reson*. 2000;144:96-107.

31. Rose JN, Nielles-Vallespin S, Ferreira PF, Firmin DN, Scott AD, Doorly DJ. Novel insights into in-vivo diffusion tensor cardiovascular magnetic resonance using computational modeling and a histology-based virtual microstructure. *Magn Reson Med*. 2019;81:2759-2773.

32. Stejskal EO. Use of spin echoes in a pulsed magnetic-field gradient to study anisotropic, restricted diffusion and flow. *J Chem Phys*. 1965;43:3597-3603.

33. Yablonskiy DA, Sukstanskii AL. Theoretical models of the diffusion weighted MR signal. *NMR Biomed*. 2010;23:661-681.

34. Torrey HC. Bloch equations with diffusion terms. *Phys Rev*. 1956;104:563-565.

35. Pope SB. *Turbulent Flows*. Cambridge, UK: Cambridge University Press; 2000.

36. Kundu PK, Cohen IM, Dowling DR. Turbulence. In: Kundu PK, Cohen IM, Dowling DR, eds. *Fluid Mechanics*. 6th ed. Waltham, MA: Elsevier; 2016: 603-697.

37. Stepišnik J. Time-dependent self-diffusion by NMR spin-echo. *Phys Rev B Phys Condens Matter*. 1993;183:343-350.

38. Mittal R, Simmons SP, Udaykumar HS. Application of large-eddy simulation to the study of pulsatile flow in a modeled arterial stenosis. *J Biomech Eng*. 2001;123:325-332.

39. Varghese SS, Frankel SH, Fischer PF. Direct numerical simulation of stenotic flows. Part 1. Steady flow. *J Fluid Mech*. 2007;582:253-280.

40. Paul MC, Molla MM. Investigation of physiological pulsatile flow in a model arterial stenosis using large-eddy and direct numerical simulations. *Appl Math Model*. 2012;36:4393-4413.

41. Ahmed SA. An experimental investigation of pulsatile flow through a smooth constriction. *Exp Therm Fluid Sci*. 1998;17:309-318.

42. Kim BM, Corcoran WH. Experimental measurements of turbulence spectra distal to stenoses. *J Biomech*. 1974;7:335-342.

43. Paulsen PK, Nygaard H, Hasenkam JM, Gormsen J, Stødkilde-Jørgensen H, Albrechtsen O. Analysis of velocity in the ascending aorta in humans. *Int J Artif Organs*. 1988;11:293-302.

44. Stein PD, Sabbah HN. Turbulent blood-flow in ascending aorta of humans with normal and diseased aortic valves. *Circ Res*. 1976;39:58-65.

45. Tobin RJ, Chang ID. Wall pressure spectra scaling downstream of stenoses in steady tube flow. *J Biomech*. 1976;9:633-640.

46. Jabir E, Lal SA. Numerical analysis of blood flow through an elliptic stenosis using large eddy simulation. *Proc Inst Mech Eng H*. 2016;230:709-726.

47. Mancini V, Bergersen AW, Vierendeels J, Segers P, Valen-Sendstad K. High-frequency fluctuations in post-stenotic patient specific carotid stenosis fluid dynamics: a computational fluid dynamics strategy study. *Cardiovasc Eng Technol*. 2019;10:277-298.

48. The International Association for the Properties of Water and Steam (IAPWS). Release on the IAPWS formulation 2008 for the thermodynamic properties of seawater. *IAPWS*. 2008:1-19. https://wiki.anton-paar.com/us-en/whole-blood/. Accessed October 16, 2020.

49. Dyverfeldt P, Kvitting J-PE, Sigfridsson A, Engvall J, Bolger AF, Ebbers T. Assessment of fluctuating velocities in disturbed cardiovascular blood flow: in vivo feasibility of generalized phase-contrast MRI. *J Magn Reson Imaging*. 2008;28:655-663.

50. Deshpande MD, Giddens DP. Turbulence measurements in a constricted tube. *J Fluid Mech*. 1980;97:65.

51. Petersson S. *Simulation of Phase Contrast MRI Measurements from Numerical Flow Data*. [Dissertation]. Linköping, Sweden: Department of Biomedical Engineering, Linköpings Universitet; 2008.

52. Dillinger H, Walheim J, Kozerke S. On the limitations of echo planar 4D flow MRI. *Magn Reson Med*. 2020;84:1806-1816.

53. Gosman A, Ioannides E. Aspects of computer simulation of liquid-fueled combustors. *J Energy*. 1983;7:482-490.

54. Petersson S, Dyverfeldt P, Gårdhagen R, Karlsson M, Ebbers T. Simulation of phase contrast MRI of turbulent flow. *Magn Reson Med*. 2010;64:1039-1046.

55. Ha H, Park KJ, Dyverfeldt P, Ebbers T, Yang DH. In vitro experiments on ICOSA6 4D flow MRI measurement for the quantification of velocity and turbulence parameters. *Magn Reson Imaging*. 2020;72:49-60.

56. Binter C, Gülan U, Holzner M, Kozerke S. On the accuracy of viscous and turbulent loss quantification in stenotic aortic flow using phase-contrast MRI. *Magn Reson Med*. 2016;76:191-196.

57. Hasenkam JM, Nygaard H, Giersiepen M, Reul H, Stødkilde-Jørgensen H. Turbulent stress measurements downstream of six mechanical aortic valves in a pulsatile flow model. *J Biomech*. 1988;21:631-645.

58. Stankovic Z, Allen BD, Garcia J, Jarvis KB, Markl M. 4D flow imaging with MRI. *Cardiovasc Diagn Ther*. 2014;4:173-192.

59. Hennel F, Michael ES, Pruessmann KP. Improved gradient waveforms for oscillating gradient spin-echo (OGSE) diffusion tensor imaging. *NMR Biomed*. 2021;34:e4434.

60. Mofakham AA, Ahmadi G. On random walk models for simulation of particle-laden turbulent flows. *Int J Multiph Flow*. 2020;122:103157.

61. Matida EA, Finlay WH, Lange CF, Grgic B. Improved numerical simulation of aerosol deposition in an idealized mouth-throat. *J Aerosol Sci*. 2004;35:1-19.

SUPPORTING INFORMATION

Additional supporting information may be found in the online version of the article at the publisher's website.

FIGURE S1 Depiction of the computational mesh used in the Large Eddy Simulation

FIGURE S2 Comparison of velocity profiles of own simulation relative to published DNS results[2] for Re = 1000. The velocity profiles are given along the normalized radius r/R for normalized velocity u/U for four positions $Z = z/D = \{0, 1, 7, -2\}$. Velocity profiles of the two approaches agree

FIGURE S3 Imaged standard deviation σ_{zz} and its distribution due to mean velocity only. As the simulation employs massless tracer particles, the images σ_{zz} correspond to spatial mean velocity gradients (highlighted by black arrows in Velocity Gradient and Standard Deviation images). Of note, σ_{zz} due to mean velocity gradients does not depend on the VEG frequency f_{VEG} as opposed to σ_{zz} due to random motion as demonstrated in the main manuscript

FIGURE S4 Definition of VCG waveforms is based on their maximum first moment over encoding time

$$\max_t \left(M_1(t) \right) = \int_{t_0}^{t_0+t} G(t)(t-t_0)\, \mathrm{d}t \qquad \text{corresponding to}$$

$$v_{enc} = \frac{\pi}{\gamma \max_t \left(M_1(t) \right)}. \quad M_1(t_{dur}) = 0 \quad \text{is equivalent to}$$

$M_1(\text{TE}) = 0$ as no readout was simulated. The VCG waveform with lowest $f_{VCG} = 100\,\text{Hz}$ was repeated for $N_{f_{VCG,100}} = 2$

VIDEO S1 Depiction of the input data for the MRI simulation as output by the Large Eddy Simulation. The data includes mean velocity components in x,y,z direction, mean velocity magnitude, Cholesky factorized IVSD and eddy frequency

VIDEO S2 Example of the MRI simulation running over time (moving green bar marks current simulation time). The particles move during the simulation time span according to their mean and fluctuating velocity. Compared to the main manuscript, the number of particles have been reduced for visualization purposes

APPENDIX

Derivation of the ensemble mean phase

If a Gaussian distribution with first and second order moments different from zero ($n = \{1, 2\}$) is assumed, Equation (3) can be simplified to

$$E(t) = \exp\left[\underbrace{-\int_0^t \langle \mathrm{j}\varphi(t_1) \rangle \, \mathrm{d}t_1}_{1} + \underbrace{\frac{1}{2} \int_0^t \int_0^t \langle \mathrm{j}\varphi(t_1)\, \mathrm{j}\varphi(t_2) \rangle_{\mathrm{LC}} \mathrm{d}t_1 \mathrm{d}t_2}_{2} \right]. \tag{A1}$$

Assuming a stationary ensemble, the integral and ensemble average of term 1 in Equation (A1) is given as

$$\int_0^t \langle \mathrm{j}\varphi(t_1) \rangle \, \mathrm{d}t_1 = \mathrm{j}\gamma \int_0^t \overrightarrow{G}(t') \cdot \overrightarrow{r}(t') \mathrm{d}t'. \tag{A2}$$

Term 2 in Equation (A1) can be written as[27]

$$\langle \mathrm{j}\varphi(t_1)\, \mathrm{j}\varphi(t_2) \rangle_{\mathrm{LC}} = \langle \mathrm{j}\varphi(t_1)\, \mathrm{j}\varphi(t_2) \rangle - \langle \mathrm{j}\varphi(t_1) \rangle \langle \mathrm{j}\varphi(t_2) \rangle, \tag{A3}$$

where the first term on the RHS is given as

$$\langle \mathrm{j}\varphi(t_1)\, \mathrm{j}\varphi(t_2) \rangle = -\gamma^2 \int_0^t \int_0^t \overrightarrow{G}(t_1) \cdot \overline{\overrightarrow{r}(t_1)\,\overrightarrow{r}(t_2)} \cdot \overrightarrow{G}(t_2) \, \mathrm{d}t_1 \mathrm{d}t_2 \tag{A4}$$

and the second term, again, assuming a stationary ensemble with $\langle \mathrm{j}\varphi(t_1) \rangle = \langle \mathrm{j}\varphi(t_2) \rangle$, results in

$$\langle \mathrm{j}\varphi(t_1) \rangle \langle \mathrm{j}\varphi(t_2) \rangle = \left[\gamma \int_0^t \overrightarrow{G}(t') \cdot \overrightarrow{r}(t') \mathrm{d}t' \right]^2. \tag{A5}$$

The location correlation[23] in Equation (A3) is denoted by index LC and corresponds to the definition of the standard deviation ($\sigma^2 = \langle w^2 \rangle - \langle w \rangle^2$ or $\sigma^2 = \mathbb{E}(w^2) - \mathbb{E}(w)^2$). Combination of Equations (A4) and (A5) results in an expression for the signal of an ensemble of magnetization with Gaussian distribution according to

$$E(t) = \exp\left[-\mathrm{j}\, \underbrace{\gamma \int_0^t \overrightarrow{G}(t') \cdot \overrightarrow{r}(t') \mathrm{d}\tau}_{\varphi_0(t) + \varphi_v(t)} - \underbrace{\frac{1}{2}\gamma^2 \int_0^t \int_0^t \overrightarrow{G}(t_1) \cdot \overline{\overrightarrow{r}(t_1)\,\overrightarrow{r}(t_2)}_{\mathrm{LC}} \cdot \overrightarrow{G}(t_2) \, \mathrm{d}t_1 \mathrm{d}t_2}_{\alpha(t)} \right]. \tag{A6}$$

Autocorrelation function of turbulent flow

As defined in the main manuscript, the autocorrelation of a random process u is given by

$$R(t_1, t_2) = \langle u(t_1)\, u(t_2) \rangle, \tag{A7}$$

where the angle brackets denote the mean (in ergodic processes either ensemble or temporal). In the case of a stationary random process only the time difference $\tau = t_2 - t_1$ matters resulting in

$$R(\tau) = \langle u(t)\, u(t + \tau) \rangle. \tag{A8}$$

Following Kundu et al,[36] the normalized autocorrelation function is defined as

$$r(\tau) = \frac{\langle u(t_1)\, u(t_2) \rangle}{\langle u^2 \rangle}. \tag{A9}$$

If the autocorrelation function decays to zero for infinite times, it is possible to define the convergent integral

$$\tau_c = \int_0^\infty r(\tau)\mathrm{d}\tau. \tag{A10}$$

If the random variable of interest is the vector-valued velocity, the two-point velocity autocorrelation function (VACF) can be defined as

$$VACF_{m,n}(\tau) = \langle u'_m(t)\, u'_n(t + \tau) \rangle, \tag{A11}$$

where $u'_{m,n}$ denote the velocity fluctuations for spatial indices m, n. The two-point cross correlation of the velocity fluctuation forms a Fourier transform pair with the Lagrangian energy spectrum $E(\omega)$

$$E_{m,n}(\omega) = \frac{1}{2\pi} \int_{-\infty}^\infty R_{m,n}(\tau)\, \mathrm{e}^{-\mathrm{j}\omega\tau} \mathrm{d}\tau \tag{A12}$$

$$R_{m,n}(\tau) = \int_{-\infty}^\infty E_{m,n}(\omega)\, \mathrm{e}^{\mathrm{j}\omega\tau} \mathrm{d}\omega. \tag{A13}$$

The kinetic energy of turbulent fluctuations per unit mass[35] is defined as

$$k = \frac{1}{2} \langle u'_m u'_m \rangle = \frac{1}{2} \langle u'^2_m \rangle, \tag{A14}$$

which has the unit $[k] = 1 \, \text{m}^2/\text{s}^2$. The turbulent kinetic energy as used in 4D Flow MRI literature is defined as

$$TKE = \rho k = \frac{\rho}{2} \left\langle u_m'^2 \right\rangle, \tag{A15}$$

where ρ is the density and $[TKE] = 1 \frac{\text{J}}{\text{m}^3}$.

It is found by setting $\tau = 0$ and $m = n$

$$\left\langle u_m'^2 \right\rangle = \int_{-\infty}^{\infty} E_{m,m}(\omega) \, d\omega, \tag{A16}$$

$$k = \int_{0}^{\infty} E_{m,m}(\omega) \, d\omega, \tag{A17}$$

such that TKE per unit mass corresponds to the area under the Lagrangian energy spectrum curve. This emphasizes the importance of probing the VACF spectrum to its full extent in order to quantitatively estimate TKE in 4D Flow MRI.

Derivation of spectrum

Starting with the expression for $\alpha(t)$ given in Equation (5) (repeated here for convenience)

$$\alpha(t) = \frac{1}{2}\gamma^2 \int_0^t \int_0^t \vec{q}(t) \cdot \overline{\vec{v}(t)\,\vec{v}(t+\tau)}_{LC} \cdot \vec{q}(t+\tau) \, d\tau, \tag{A18}$$

the factors can be permuted using the rule $b \otimes (Ta) = (b \otimes a)T^{\mathrm{T}}$, where the symmetry of the velocity autocorrelation function matrix $\overline{\vec{v}(\tau_1)\,\vec{v}(\tau_2)}_{LC} = \left(\overline{\vec{v}(\tau_1)\,\vec{v}(\tau_2)}_{LC} \right)^{\mathrm{T}}$ is leveraged by inserting of Equation (9) into Equation (A18);

$$\alpha(t) = \frac{1}{2\pi}\gamma^2 \int_0^t \int_0^t \vec{q}(t)\,\vec{q}(t+\tau) \int_{-\infty}^{\infty} D_{m,n}(\omega)e^{j\omega\tau} d\tau \, d\omega. \tag{A19}$$

Assuming gradient signals of limited energy and being deterministic, the Wiener-Khintchine theorem can be applied yielding

$$\int_{-\infty}^{\infty} \underbrace{\vec{q}^{\,*}(t)\,\vec{q}(t+\tau)}_{R_q(\tau)} d\tau = \frac{1}{2} \int_{-\infty}^{\infty} |q(\omega,t)|^2 \, e^{j\omega t} d\omega, \tag{A20}$$

where the complex conjugate can be neglected since the integrated gradient waveforms are real-valued. Therefore, it is found that the autocorrelation function $R_q(\tau)$ of the gradient is given by the absolute Fourier coefficients $q(\omega, t)$ being squared resulting in the expression for $\alpha(t)$ as in Equation (10) with

$$S(\omega, t) = |q(\omega, t)|^2. \tag{A21}$$

Self-similar flows, Reynolds number, viscosity

When comparing different flow scenarios, the dimensionless Reynolds number

$$Re = \frac{ud}{\nu} \tag{A22}$$

is used, where u, d and ν are the mean inlet velocity, the unoccluded diameter and the dynamic viscosity, respectively. For self-similar flows, if the Reynolds number is kept the same, the resulting solution will be the same for appropriately scaled (= normalized) variables.[35] Of note, this enables one to compare experiments with eg, different viscosities if the Reynolds number is equal by using appropriately scaled velocity variables. Important to note, however, is that non-normalized variables such as TKE and eddy frequency *are not comparable* without prior scaling. Therefore, simulations conducted with same *Re* but smaller viscosity will exhibit smaller TKE than those with higher values of viscosity.

The dimensionless Strouhal number

$$St = \frac{2\pi f d}{u} \tag{A23}$$

is used as normalized "frequency" axis in CFD spectra plots (eg, Refs. [39] and [46]), where f, d and u are the non-normalized frequency, minimum diameter (stenotic throat) and mean velocity at the stenosis throat (eg, 4× mean inlet velocity for 75% reduction in area).

However, when changing viscosity but *Re* number and *Str* axis remain unchanged, one finds the non-normalized frequency axis f to be scaled by viscosity. Of note, this changes f_{eddy} at which eg, the inertial range starts. The transition frequency f_{eddy} is of great importance for encoding theory discussed in the main manuscript.

Particle equations of motion

The equations of motion for an inert particle model are given by[61]

$$\frac{du_p}{dt} = F_D (u - u_p) + g_x \frac{\rho_p - \rho}{\rho_p} + F_x, \tag{A24}$$

where the first RHS term denotes the drag force per unit particle mass and

$$F_D = \frac{18\mu}{\rho_p d_p^2} \frac{C_D Re_p}{24}, \tag{A25}$$

where u, u_p, μ, ρ, ρ_p, d_p, Re_p and C_D is fluid phase velocity, particle's velocity, molecular viscosity of the fluid,

fluid density, particle density, particle diameter, particle Reynolds number and drag coefficient, respectively. Previous works have shown that these parameters have an influence on particle dynamics.[61] As F_D essentially describes how fast the particle would adjust its velocity to the fluid velocity, the particle's trajectory is affected by the set parameters, especially for particle tracing in turbulent flow. In the current manuscript, massless tracer particles have been used. On one hand, this does not use any assumptions on particle parameters, on the other hand, due to instantaneous velocity changes due to $u - u_p$, in the MRI simulation, spatial gradients in the mean velocity field will result in increased levels of imaged turbulence. This is discussed in the main manuscript in the mean velocity variation (MVV) section and accounted for in the Results section.